

Multistate magnetic tunnel junction based on a single two-dimensional van der Waals antiferromagnet

Jie Yang^{1,*}, Baochun Wu^{2,†}, Sichun Zhao¹, Shiqi Liu^{3,†}, Jing Lu^{4,5,6,‡}, Shunfang Li¹, and Jinbo Yang^{4,5,6,§}

¹Key Laboratory of Material Physics, Ministry of Education, School of Physics, Zhengzhou University, Zhengzhou 450001, P. R. China


²State Key Laboratory of Low Dimensional Quantum Physics and Department of Physics, Tsinghua University, Beijing 100871, P. R. China

³State Key Laboratory of Spintronics Devices and Technologies, Hangzhou 311305, P. R. China

⁴State Key Laboratory for Artificial Microstructure and Mesoscopic Physics and School of Physics, Peking University, Beijing 100871, P. R. China

⁵Beijing Key Laboratory for Magnetoelectric Materials and Devices (BKL-MEMD), Peking University, Beijing 100871, P. R. China

⁶Yangtze Delta Institute of Optoelectronics, Peking University, Nantong 226010, P. R. China

 (Received 28 December 2023; revised 26 April 2024; accepted 6 June 2024; published 9 July 2024)

Antiferromagnets are emerging as promising competitors for advanced multistate memories because of their ignorable stray fields, ultrafast resonance dynamics and, especially, the rich variety of spin-order responses. Motivated by the determination of stripy intralayer antiferromagnetic order and the exceptional ambient stability of two-dimensional (2D) CrOCl, we here propose a single-basement magnetic tunnel junctions (MTJs) composed of 2D intralayer antiferromagnets and predict the spin-resolved transport properties represented by Ag/CrOCl/Ag MTJs. Using *ab initio* quantum-transport simulations, four different resistance states are demonstrated in 2D CrOCl-based MTJs with the magnetic order of CrOCl evolving from antiferromagnetism, followed by different metamagnetic arrangements and, finally, to ferromagnetism. The resistance area is remarkably low (only 0.02–0.2 $\Omega \mu\text{m}^2$) in the Ag/monolayer CrOCl/Ag MTJ, indicating high energy efficiency. The calculated tunneling magnetoresistance generated between any magnetic order and the ground antiferromagnetic order reaches an impressive range of 110% to 900% and 410% to 48 000% for the monolayer and bilayer CrOCl-based MTJ, respectively, at zero bias and decreases as the bias increases. Our work also provides an insightful idea for using metamagnetic transitions and the related multiple conductance effect in 2D intralayer antiferromagnets, which paves a new way for future nonvolatile energy-efficient multiple-state memory devices.

DOI: [10.1103/PhysRevApplied.22.014017](https://doi.org/10.1103/PhysRevApplied.22.014017)

I. INTRODUCTION

Recently, antiferromagnets are emerging as an alternative to ferromagnets for spintronic applications. Antiferromagnets are robust against magnetic perturbations, produce no stray fields, exhibit ultrafast spin dynamics and, thus, could potentially serve as highly reliable, high-density, rapid-response, and multiple-state information carriers [1,2]. Together with the rapid development of two-dimensional (2D) technology, numerous spintronic

devices composed of the 2D van der Waals (vdW) antiferromagnets with enormous tunneling magnetoresistance (TMR) have been reported [3,4]. One of the most remarkable findings arises from the antiferromagnetic 2D CrI₃-based magnetic tunnel junctions (MTJs), which generate TMR of 95%–1 000 000% with 2–10-layer CrI₃ included [5,6]. This prominent transport behavior gives sufficient confidence to pursue nonvolatile memory based on 2D antiferromagnets. However, previous research on MTJs is mainly focused on the interlayer antiferromagnetic (AFM) semiconductors and TMR induced by two-state switching (antiferromagnetic and ferromagnetic states), while the resistance difference resulting from multiple metamagnetic transitions in the 2D antiferromagnets, such as the spin-flop moment arrangements in the odd-layer CrCl₃ and the few-layer CrPS₄, were seldom considered in devices [7–10]. Upon combining the rich magnetic orders

*Contact author: yangjie_phy@zzu.edu.cn

†Contact author: liushiqi@spinlab.cn

‡Contact author: jinglu@pku.edu.cn

§Contact author: jbyang@pku.edu.cn

¶These authors contributed equally.

with the spin-dependent tunneling channels together, multiple resistance states are reasonably expected to be displayed once different spin configurations are switched in sequence when made into devices. Thus, the 2D antiferromagnet can be an ideal platform for exploring prototype devices of multiple-state memories composed of only one magnetic candidate.

Bulk CrOCl is known as an air-stable vdW AFM semiconductor. Its stability is confirmed to be maintained even for its monolayer (ML) [11]. Distinct from the layer-by-layer engineered magnetism of CrI₃, 2D CrOCl exhibits an intralayer AFM coupling arrangement (insusceptible to layers), which has not been correctly described in most previous theoretical works [12–14]. The ground AFM order of the 2D CrOCl is stripy within each layer along the *b*-axis, with an out-of-plane magnetic anisotropy [Fig. 1(a)] as verified by the neutron powder diffraction [15]. Recently, a series of unconventional magnetic phases and transitions in the 2D CrOCl are detected with the magnetic order evolving from the AFM, spin-flop, ferrimagnetic (ferri) and, finally, to the ferromagnetic (FM) state [Fig. 1(c)] in sequence, as the magnetic field increases from 0 to 20 T [16,17]. FeOCl, VOCl, DyOCl, and other isostructural compounds are also reported to be suitable for appealing metamagnetic transitions [18–20]. The 2D limit CrOCl, with distinct spin configurations and definite stability, is chosen from these isostructures as the typical prototype for polymorphic storage.

Although the tunneling devices constituted by graphite electrodes and CrOCl flakes have been artificially constructed [16], the internal physical understanding and analysis of multiple resistance states remain unclear. In this work, we investigate multiple resistance states associated with the TMR in Ag/ML CrOCl/Ag and Ag/bilayer (BL) CrOCl/Ag MTJs by employing *ab initio* quantum-transport simulations. After elucidating the spin-resolved transport properties of the MTJs, we identify four different resistance states, which are consistent with the multistate memory we have envisaged above. A remarkably low resistance area (RA) of only 0.02–0.2 Ω μm² is observed in the Ag/ML CrOCl/Ag MTJ, which stems from the small Schottky barrier of about 0.28 eV in the Ag/CrOCl interface (see Fig. S1 in the Supplemental Material [26]) that indicates the high energy efficiency. The RAs of the four states in the Ag/BL CrOCl/Ag MTJ are in the range of 0.84–399 Ω μm², larger than that of the ML counterpart because of the thicker barrier. The generated TMR, linked to the transition from the initial AFM state to the FM state, is around 100%–1000% and 400%–50 000% for the ML and BL CrOCl-based MTJ, respectively, and decreases with the applied bias. The low RA product and the remarkable resistance difference of the 2D CrOCl-based MTJ uncover the promising potential of 2D antiferromagnetic CrOCl and its isostructural compounds in the applications of future energy-efficient multistate memories.

II. METHODOLOGY

The geometric and electronic structure calculations of the ML and BL CrOCl are carried out using the projector-augmented wave method implemented in the VIENNA *AB INITIO* SIMULATION PACKAGE (VASP) [21]. The Perdew-Burke-Ernzerhof (PBE) generalized gradient approximation (GGA) is adopted to describe the exchange-correlation functional [22–24]. A sufficient vacuum thickness (i.e., 20 Å) along the *z*-axis is adopted to eliminate the interactions between adjacent unit cells. The Monkhorst-Pack *k*-point mesh is sampled with a separation of about 0.01 Å⁻¹ in the 2D Brillouin zone. The cutoff energy is set at 700 eV for the plane-wave basis expansion with the total energy convergence criteria of 1 × 10⁻⁴ eV. The ionic relaxation for structure optimization stops when the residual force on each atom is less than 0.01 eV·Å⁻¹. The opt86-vdW functional is used to consider the interlayer vdW corrections. The Liechtenstein +*U* method in VASP reaches the accuracy we expected (see details in the Supplemental Material [25,26]). The on-site Coulomb interaction *U* with the Liechtenstein version for the Cr *d* orbitals are set at *U* = 3.0 eV and *J* = 1.0 eV, respectively, which have been tested in previous calculations of the magnetic ground state of CrOCl [16].

The spin-resolved transport behaviors of the 2D CrOCl-based MTJs are calculated by the density-functional theory (DFT) coupled with nonequilibrium Green's function (NEGF) within the QUANTUMATK package [27]. Collinear and noncollinear GGA represent the exchange-correlation potential herein in the form of the PBE potential. The hybrid function has a limited impact and does not alter the qualitative results (see details in Fig. S5 and its discussion in the Supplemental Material [26]). The double zeta polarized basis set is selected for the calculations. The real-space mesh cutoff is taken as 155 hartree. The *k*-point meshes for the electrode region and the central tunneling region are 5 × 9 × 108 and 5 × 9 × 1, respectively. The boundary conditions in the central zone are periodic along the *x*- and *y*-direction and are Dirichlet along the *z*-direction. The boundary conditions in the electrode zone are periodic along the *x*-, *y*-, and *z*-direction. Spin-orbit coupling is not included in our device calculations (see details in Fig. S6 in the Supplemental Material [26]).

In our calculations, the transmission coefficient $T_{\sigma}^{k_{//}}(E)$ is expressed as follows [28]:

$$T_{\sigma}^{k_{//}}(E) = \text{Tr}[n_{\sigma} \Gamma_{l,\sigma}^{k_{//}}(E) G_{\sigma}^{k_{//}}(E) \Gamma_{r,\sigma}^{k_{//}}(E) G_{\sigma}^{k_{//}\dagger}(E)],$$

where $k_{//}$ is the reciprocal lattice vector along the surface-parallel direction in the irreducible Brillouin zone given a certain energy, σ denotes the spin index, n_{σ} is the density matrix in the spin Hilbert space containing two spin elements ($n_{\sigma} = 1$ in collinear cases, otherwise $n_{\sigma} \neq 1$ in noncollinear situations), $G_{\sigma}^{k_{//}}(E)$ and $G_{\sigma}^{k_{//}\dagger}(E)$ represent

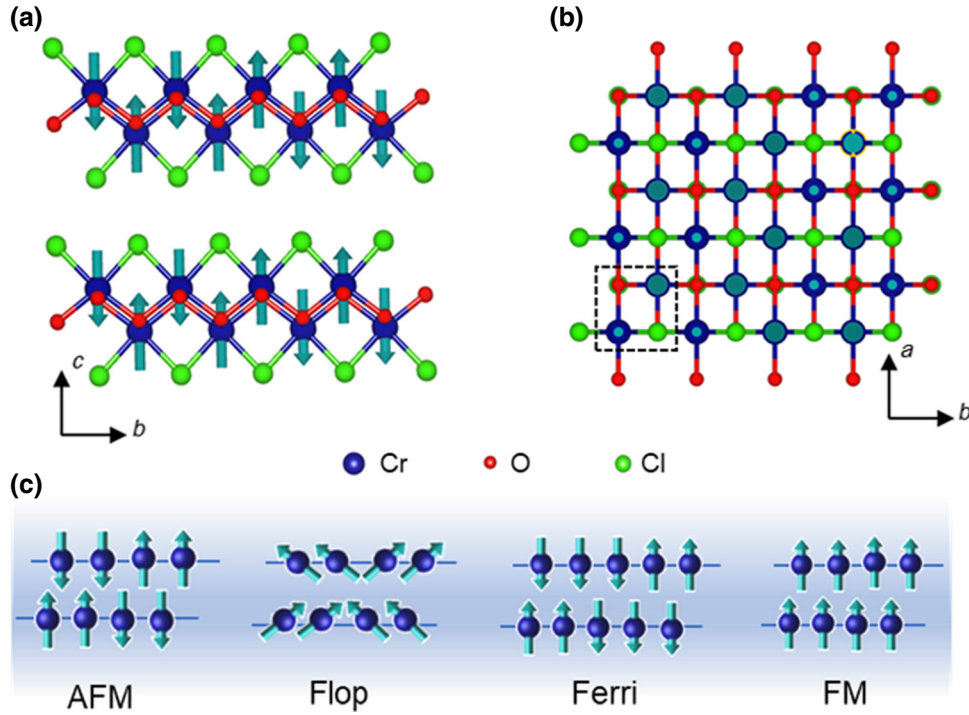


FIG. 1. Geometry structure and spin configurations of CrOCl. (a) Side view and (b) top view of the layered CrOCl. Green arrows show the stripy antiferromagnetic order. The black dashed square labels the geometric primitive cell. (c) Diagrams of four spin configurations of monolayer CrOCl. Blue balls display Cr atoms in two staggered Cr-O layers of each CrOCl layer. Arrows show the direction of magnetic moments.

the retard and advanced Green's function, respectively, and $\Gamma_{l/r,\sigma}^{k_{//}}(E) = i \left(\sum_{l/r,\sigma}^{k_{//}} - \sum_{l/r,\sigma}^{k_{//}\dagger} \right)$ is the imaginary part of the self-energy indicating the coupling between the left or right electrode and the center region. The formalism $G_{\sigma}^{k_{//}}(E)$ is written as follows [29]:

$$G_{\sigma}^{k_{//}}(E) = \frac{1}{(E + i\delta_{+})IH^{k_{//}} - \sum_{l,\sigma}^{k_{//}}(E) - \sum_{r,\sigma}^{k_{//}}(E)},$$

where δ_{+} is an infinitesimal positive number, I is the identity matrix, $H^{k_{//}}$ is the Hamiltonian matrix, and $\sum_{l/r,\sigma}^{k_{//}}(E)$ is the self-energy matrix. The transport current is calculated following the Landauer-Büttiker equation [30,31], i.e.,

$$I_{\sigma}(V_b) = \frac{e}{h} \int_{-\infty}^{+\infty} \{T_{\sigma}(E, V_b)[f(E - \mu_L) - f(E - \mu_R)]\} dE,$$

where $T_{\sigma}(E, V_b)$, f , $\mu_{L/R}$, are the averaged $T_{\sigma}^{k_{//}}(E)$ over all the different $k_{//}$, the Fermi-Dirac distribution function, the Fermi level of the left or right electrode, respectively.

III. RESULTS

A. Basics of the 2D CrOCl

As shown in Figs. 1(a) and 1(b), each layer of CrOCl consists of double staggered Cr-O layers sandwiched by two Cl atoms. Linear Cr atom chains are connected by O atoms run along the b -axis. The vdW force contacts the neighboring layers along the c -axis. The lattice parameters of the ML and BL CrOCl are $a = 3.182 \text{ \AA}$ and $b = 3.863 \text{ \AA}$. As CrOCl is an intralayer antiferromagnet, the magnetic order in the ML and BL CrOCl is the same as that in crystal [2]. The magnetic moment of each Cr^{3+} is oriented to the c -axis and arranged in the AFM state ($\uparrow\uparrow\downarrow\downarrow$) along the b -axis, forming a magnetic unit cell composed of a fourfold original unit cell (Fig. 1), verified by both experimental observation and theoretical prediction [15,16,19]. When an external magnetic field (i.e., where $\mathbf{H} \parallel c$) is applied, metamagnetic behavior is manifested in the 2D CrOCl system [16,17]. Specifically, first, the spins of Cr^{3+} are rotated perpendicular to the field direction due to the *spin-flop* transition [hereafter referred to as the flop state, as shown in Fig. 1(c)]. The flop state appears to compensate for the field-driven reorientation for a suddenly increasing effective anisotropic energy caused by the external magnetic field (details in Fig. S4 in the Supplemental Material [26]). This metastable state in 2D CrOCl was observed by the experiment. [32,33]. To again prove it is a metastable state,

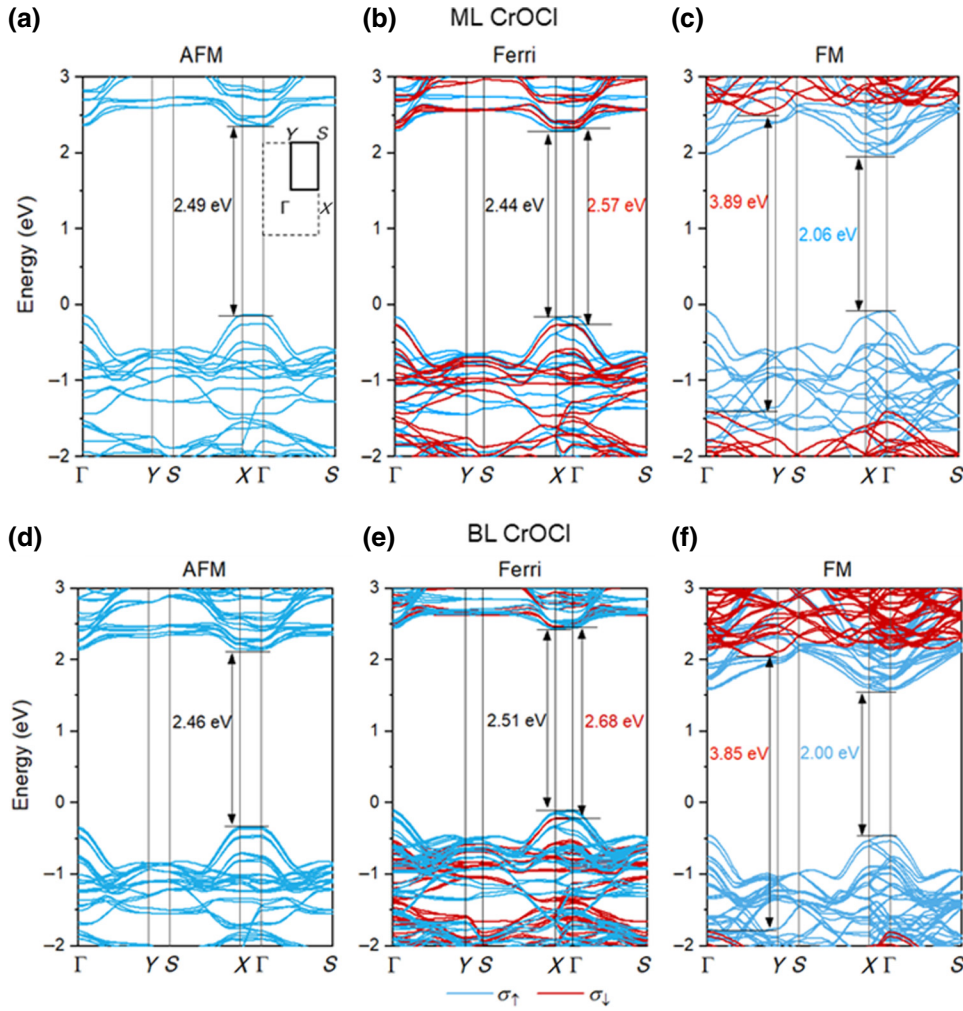


FIG. 2. Spin-resolved band structures of (a)–(c) monolayer and (d)–(f) bilayer CrOCl under different magnetic orders. The Fermi level is set to zero. From the left to the right panel, the magnetic orders are antiferromagnetism (AFM), ferrimagnetism (Ferri), and ferromagnetism (FM), respectively. Brillouin zone and k -point path are inserted in (a). A 1×4 supercell is used for the AFM and FM orders. A 1×5 supercell is used for the ferri order.

we calculate the energy of the ML CrOCl at the AFM, flop, and FM states under the noncollinear DFT framework. The E_{flop} is between E_{AFM} and E_{FM} , as shown in Table S1 in the Supplemental Material [26]. Second, the CrOCl layer experiences a second spin transition—the ferrimagnetic (Ferri) state ($\uparrow\uparrow\downarrow\downarrow$)—induced by the external magnetic field. The Ferri state has a fivefold periodicity along the b -axis [Fig. 1(c)]. Finally, when the applied magnetic field is sufficiently strong, all the spins in CrOCl align with the field direction to form the FM arrangement ($\uparrow\uparrow\uparrow$). This is the whole spin texture evolution [see Fig. 1(c)] of the 2D CrOCl under an increasing external c -axis magnetic field ranging from 0 to 20 T [15].

The semiconducting band structures and bandgaps of ML and BL CrOCl are similar, as displayed in Fig. 2. The AFM state has spin-degenerate dispersion with a bandgap of ~ 2.5 eV for both the ML and BL CrOCl, in good agreement with previous research [34]. In the Ferri and FM states, the band dispersions are spin distinctive and exhibit 100% spin polarization in both the conduction band (CB) minimum and the valence band (VB) maximum, implying large conductance once the Fermi level is tuned to either

the CB or VB energy zone. Moreover, the ferrimagnetic bandgaps for both spin-up and spin-down modes are close to that of the AFM state but with slight movement toward the Fermi level. The FM bandgaps are as large as ~ 2.0 eV for spin-up and ~ 3.9 eV for spin-down. The bandgaps get narrow and the energy range of 100% spin polarization near the Fermi level widens when the magnetic order transforms from the ground AFM to the FM state.

B. Transport behavior of AG/CrOCl/AG MTJs

To evaluate the transport behavior of CrOCl, we construct device models as shown in Figs. 3(a) and 3(b). The semi-infinite Ag (111) represents the metal electrode and contacts with CrOCl with a mismatch of less than 5%. The optimized minimum distance between CrOCl and Ag atoms is 2.82 Å. The DFT calculations show that Ag triggers a slight band hybridization effect after contacting, forming a p-type Schottky barrier of 0.28 eV with the ML CrOCl (Fig. S1 in the Supplemental Material [26]). We choose $1 \times 4 \times 1$ and $1 \times 5 \times 1$ CrOCl supercells to build

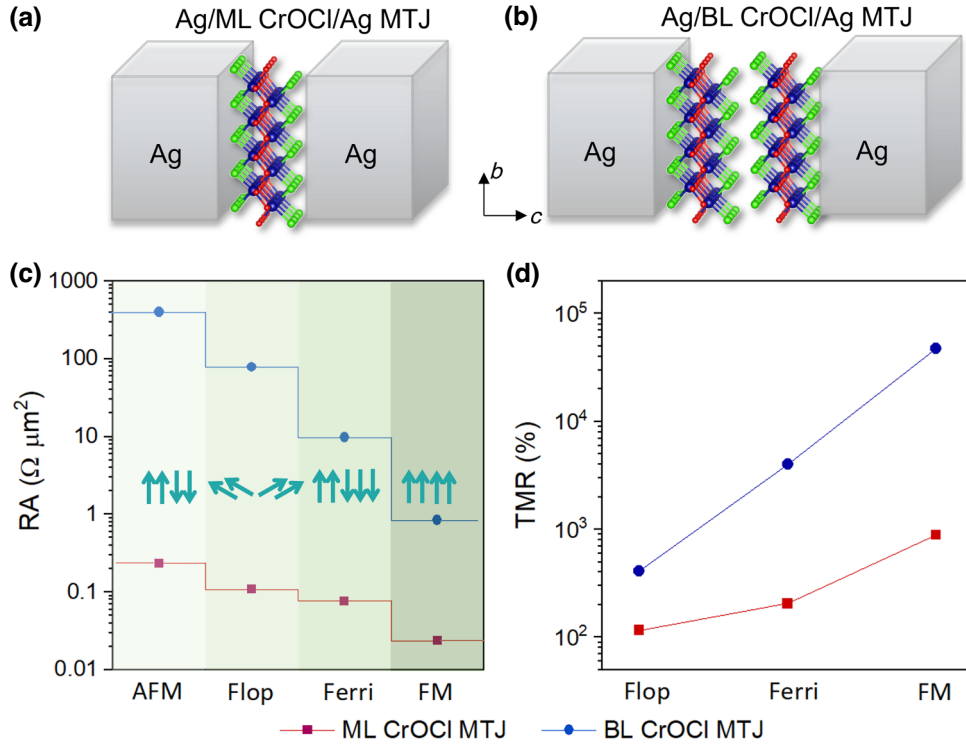


FIG. 3. Device diagram of (a) monolayer and (b) bilayer CrOCl-based magnetic tunnel junction. (c) Multiple resistance area products of CrOCl-based MTJs under different magnetic order. (d) Calculated tunneling magnetoresistance of CrOCl MTJs. RA_M stands for the resistance area under different magnetic arrangements.

Ag/CrOCl/Ag MTJs in the AFM (including FM and flop) and the Ferri states, respectively.

To make an equal comparison, we normalize the conductance G to the RA product, which is calculated by $R_{RA} = A/G = A/(T(E_F)G_0)$, where A is the transverse area of the device, $T(E_F)$ is the transmission coefficient at the Fermi level, and $G_0 = e^2/h$ is the quantum conductance. Table I summarizes the calculated RA under different spin configurations of the CrOCl-based MTJs. As shown in Fig. 3(c), when the ground AFM order is transformed to the flop state, followed by the Ferri state and, finally, to the FM state, the corresponding RA plateau gradually decreases due to the successive growth of $T(E_F)$. The RA in the ML CrOCl MTJs is only $0.02\text{--}0.2 \Omega \mu\text{m}^2$, far less than that in the Fe/MgO/Fe MTJ with a similar barrier thickness of 1 nm, which reaches several $M\Omega \mu\text{m}^2$ and severely hinders further application [35,36]. Encouragingly, the ML CrOCl might resolve the issue of a large RA product in MTJs, indicating higher-density integration and lower heat dissipation. When the magnetic tunneling barrier increases to BL CrOCl, the RA is enlarged to the range of $0.8\text{--}399 \Omega \mu\text{m}^2$, which becomes larger than the ML case under the same magnetic arrangements. For example, in the Ferri state, the RA of the BL CrOCl MTJ is $9 \Omega \mu\text{m}^2$, two orders of magnitude higher compared with the ML CrOCl case ($0.07 \Omega \mu\text{m}^2$). The reason lies in a

greater d in $T \propto e^{-(\sqrt{2(\Phi_B - E_F)/\hbar})d}$ for a thicker barrier [37], where Φ_B and d are the height and thickness of the tunneling barrier, respectively, resulting in a smaller T and, thus, a larger RA. The barrier thickness for our Ag/BL CrOCl/Ag MTJ is ~ 1.8 nm, and the corresponding RA is $0.8\text{--}399 \Omega \mu\text{m}^2$. When the Fe/MgO/Fe MTJ has the same barrier thickness, its RA is $1000\text{--}5000 \Omega \mu\text{m}^2$ [35]. Therefore, the RA product level of the BL circumstance remains lower than that of conventional Fe/MgO/Fe MTJs.

Note that the transport behavior of the AFM, Ferri, and FM states are calculated by the method of collinear spins, while the flop transport behavior is calculated via the framework of noncollinear spins, where the spin eigenstate becomes a 2×2 matrix with the mixing of majority (spin-up) and minority (spin-down) components instead of being a diagonal one (spin-up and spin-down electrons completely decoupled from each other). The noncollinear density matrix is given by the following:

$$n(r) = \sum \psi_{\uparrow}^{\dagger}(r)\psi_{\downarrow}(r) = \begin{bmatrix} n_{\uparrow\uparrow} & n_{\uparrow\downarrow} \\ n_{\downarrow\uparrow} & n_{\downarrow\downarrow} \end{bmatrix}.$$

TABLE I. Summary of the calculated transmission, resistance area (RA), and $\text{TMR}_{\text{M-AFM}}$ (magnetoresistance between any magnetic orders and the AFM order) without bias.

		AFM	Flop	Ferri	FM
Ag/ML CrOCl/Ag MTJ	$T (e^2/h)$	1.12×10^{-1}	2.42×10^{-1}	4.12×10^{-1}	1.11
	RA ($\Omega \mu\text{m}^2$)	2.35×10^{-1}	1.08×10^{-1}	7.69×10^{-2}	2.37×10^{-2}
	$\text{TMR}_{\text{M-AFM}}$	—	116%	205%	891%
Ag/BL CrOCl/Ag MTJ	$T (e^2/h)$	6.57×10^{-5}	3.34×10^{-4}	3.26×10^{-3}	3.16×10^{-2}
	RA ($\Omega \mu\text{m}^2$)	3.99×10^2	7.85×10^1	9.74	8.31×10^{-1}
	$\text{TMR}_{\text{M-AFM}}$	—	412%	4000%	48 241%

To transform $n(r)$ into the diagonal form n^{diag} , a rotation matrix U is involved so that [27,38]

$$n^{\text{diag}} = UnU^\dagger = \begin{bmatrix} n_{\uparrow\uparrow} & 0 \\ 0 & n_{\downarrow\downarrow} \end{bmatrix},$$

$$U = \begin{bmatrix} e^{i\frac{\phi}{2}} \cos \frac{\theta}{2} & e^{-i\frac{\phi}{2}} \sin \frac{\theta}{2} \\ -e^{i\frac{\phi}{2}} \sin \frac{\theta}{2} & e^{-i\frac{\phi}{2}} \cos \frac{\theta}{2} \end{bmatrix} \quad \text{and} \quad n = U^\dagger n^{\text{diag}} U,$$

where θ and ϕ are the global coordinates. In view of the matrix conversion of noncollinear spins, when θ is set to 0° or 180° (the collinear circumstance), U is a unit matrix, making $n = n^{\text{diag}}$, to which the collinear circumstance belongs. Taking the case of BL result as a typical example, the calculated R_{AFM} and R_{FM} (401 and $0.83 \Omega \mu\text{m}^2$, respectively) in the noncollinear framework, which are almost the same as those (399 and $0.83 \Omega \mu\text{m}^2$, respectively) in the collinear framework. Therefore, the discrepancy between collinear and noncollinear sets for the AFM, Ferri, or FM states is negligible. The RA we obtain in Table I and Fig. 3(c) are convincing.

The TMR [refer to $R_{\text{TMR}}(\text{M})$] is defined as follows to describe the dynamic process of magnetization in CrOCl:

$$R_{\text{TMR}}(\text{M}) = \frac{R_{\text{RA}}(\text{AFM}) - R_{\text{RA}}(\text{M})}{R_{\text{RA}}(\text{M})} \times 100\%,$$

where $R_{\text{RA}}(\text{M})$ and $R_{\text{RA}}(\text{AFM})$ are under the metamagnetic and the ground AFM states, respectively. Figure 3(d) exhibits the calculated TMR of the ML and BL situations at zero bias. Followed by the sequence of magnetization evolvment, TMR_{M} grows from 110% to 900% and 410% to 48 000% in the ML and BL case, respectively. The BL MTJ has a higher TMR than the ML for all metamagnetic states [Fig. 3(d)]. Using only ML CrOCl, the TMR_{FM} (maximum TMR) of 900% is close to the Fe/MgO/Fe limit (as high as 1000%). In the BL-CrOCl-based MTJ, a TMR_{FM} of 48 000% is theoretically two orders of magnitude larger than that of the ML CrI_3 counterpart, whose limit TMR is 600%–1500% depending on the AFM-FM switching [39,40]. The saturate field for ML and BL CrOCl to FM switching exceeds 20 T, much higher than the Fe film or the 2D CrI_3 . However, taking advantage of the flop

and the Ferri phases in the ML and BL CrOCl under a small external field (<7 T) could guarantee an impressive TMR of 110–205% and 410%–4000%, respectively, which are comparable and even significantly above the commercial reservation standards for sensitive operation ($\sim 200\%$) [41].

More importantly, in terms of achieving multistate switching, compared with multiferroic devices assembling ferromagnets, ferroelectrics, and electrodes, our MTJs need single CrOCl and electrodes, which is simple and can avoid designing asymmetric ferroelectric interfaces and bringing complex interfacial issues [42]. For example, to obtain four different resistance states, the vdW PtTe₂/Fe₄GeTe₂/In₂Se₃/Fe₃GeTe₂/PtTe₂ multiferroic tunnel junctions have to construct asymmetric ferroelectric interface engineering for In₂Se₃ (left of it is Fe₄GeTe₂ and right is Fe₃GeTe₂) and PtTe₂ electrodes are added on both sides to avoid a loss of generality [43]. The device generates four resistance states with a resistance ratio (tunneling electroresistance and TMR) of only 40%–89% [43], far less than 110%–48 000% TMR in the single CrOCl-based MTJs.

Because we applied the noncollinear-spin basis for the flop state calculation, the global coordinates— θ and ϕ for each magnetic moment (\mathbf{m}) of the Cr atom—are observable (Fig. S2 in the Supplemental Material [26]). Here, θ is the angle with the c -axis and ϕ is the polar angle in the ab -plane. In the flop state, \mathbf{m} of Cr^{3+} prefers to align with the in-plane direction with the averaged θ angle of 84° and 81° and a ϕ angle of 180° or 0° for the ML and BL CrOCl MTJ, respectively, based on our calculations. For the case of BL, the calculated θ angles of Cr atoms of stripy 1 and 4 (located near the electrodes) are similar to those in the ML case, where θ angles in stripy 2 and 3 (away from electrodes) are relatively small. The size of \mathbf{m} for each Cr atom has similar rules. Namely, \mathbf{m} of Cr atoms in Stripy 1 and 4 of the BL MTJ is $2.81 \mu_{\text{B}}$ per atom, the same as those in the ML counterpart, while \mathbf{m} in Stripy 2 and 3 is $2.78 \mu_{\text{B}}$, which is very close to $m = 2.77 \mu_{\text{B}}$ of pristine CrOCl. This slight discrepancy in direction and value of \mathbf{m} might be attributed to interfacial hybridization between two Ag electrodes and their sandwiched CrOCl layers. To verify our assumption, we perform Bader analysis and find

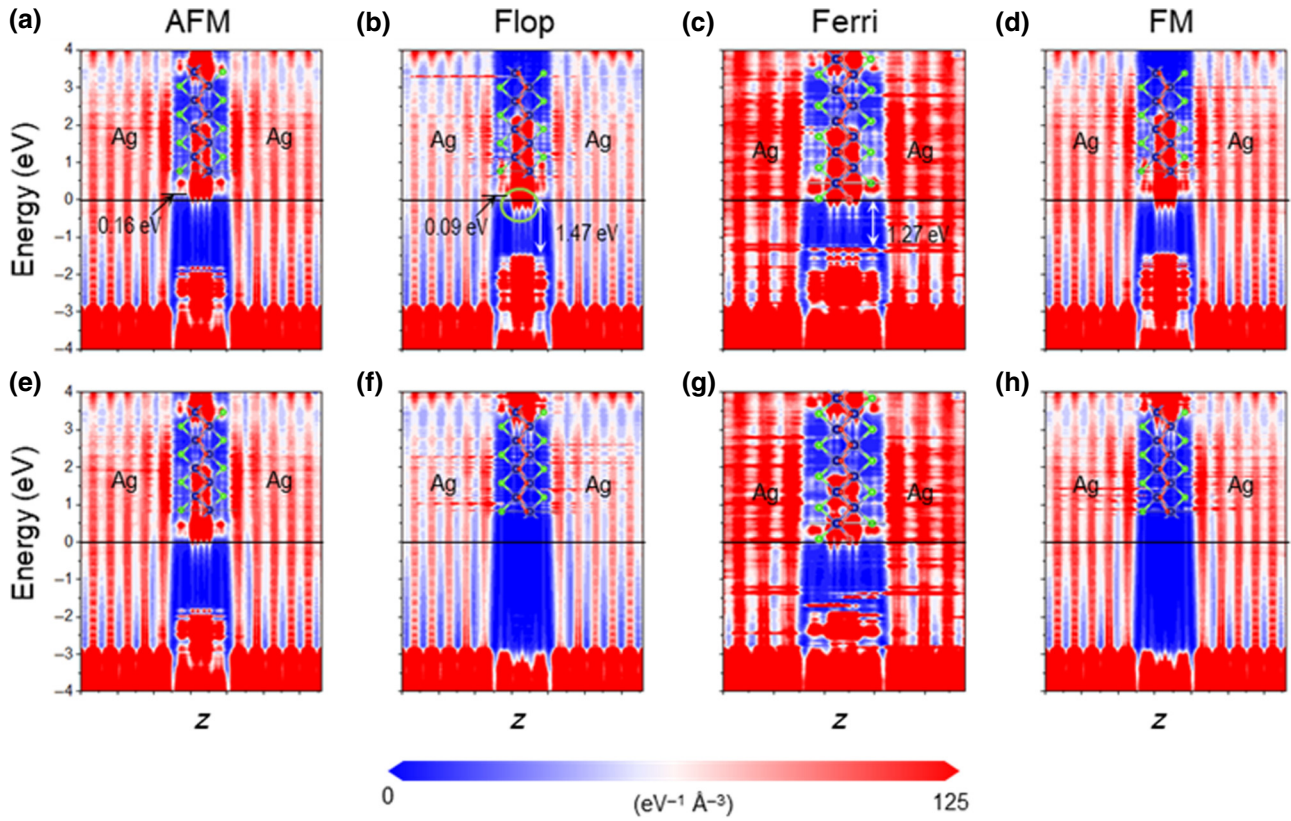


FIG. 4. Spin-resolved projected local density of states of Ag/ML CrOCl/Ag MTJs for the AFM, flop, Ferri, and FM states, respectively, for each column from left to right at zero bias. The upper and lower panels stand for spin-majority (spin-up) and minority (spin-down) channels in each magnetic state, respectively. The Fermi level is zero.

that, per CrOCl unit cell, each Ag part transfers $0.03e$ to its neighboring Cr-O layer, which effectively enhances the m of the Cr ions.

C. Projected local density of states under different magnetic arrangements

To further understand the mechanism of the desirable RA and an enormous TMR for the CrOCl-based configurations, we plot the projected local density of states (PLDOS) in four different magnetic states at zero bias for comparison, as shown in Figs. 4 and S3 in the Supplemental Material [26]. According to the z -axis PLDOS of the Ag/ML CrOCl/Ag configuration [Fig. 4(a)], the interfacial n-type Schottky barrier between Ag and the ground AFM ML CrOCl is only 0.16 eV (a bit smaller than 0.28 eV from projected band structures), resulting in high electron tunneling efficiency and, thus, a small RA. Unlike the sharp steplike barrier profile of a few-layer A-type vdW AFM tunnel region such as CrI₃ [6,40,44], the barrier outline from CrOCl is not unified within one layer. The PLDOS of CrOCl at different magnetic states appears analogous in general but diverse in detail [Figs. 4(a)–4(d) and

S3(a)–S3(d) in the Supplemental Material [26]]. Specifically, we focus on the Fermi level's dominant spin-majority states (spin-up electrons). When the ML CrOCl experiences the first transition to the flop state, compared with the AFM state, its conduction band states move down toward the Fermi level (E_f) [Figs. 4(a) and 4(b)], leading to a quasi-Ohmic contacting barrier (0.09 eV) for the spin-up channel in the conduction band. Meanwhile, the PLDOS from the staggered Cr-O layer region in the flop state ultimately crosses E_f [green circle in Fig. 4(b)], diminishing the RA of the flop state. It is worth mentioning that the mapped PLDOS in the flop state [Fig. 4(b)] only shows projected spin-majority and spin-minority states, excluding spin-scattering states. This is why the flop PLDOS exhibits fewer red states and, thus, lower color intensity than the others. When the ML CrOCl evolves into the ferrimagnetic state, the Ohmic contact with the conduction band and the reduced p-type barrier height (i.e., flop to Ferri: 1.47 eV to 1.27 eV) in the valence band both contribute to the transport possibilities. Thus, RA is further lowered. Finally, in the FM state, due to the combination of quasi-Ohmic interfacial contact and sufficient participant states for tunneling, the FM PLDOS contributes the most to the transport transmission and possesses the least RA.

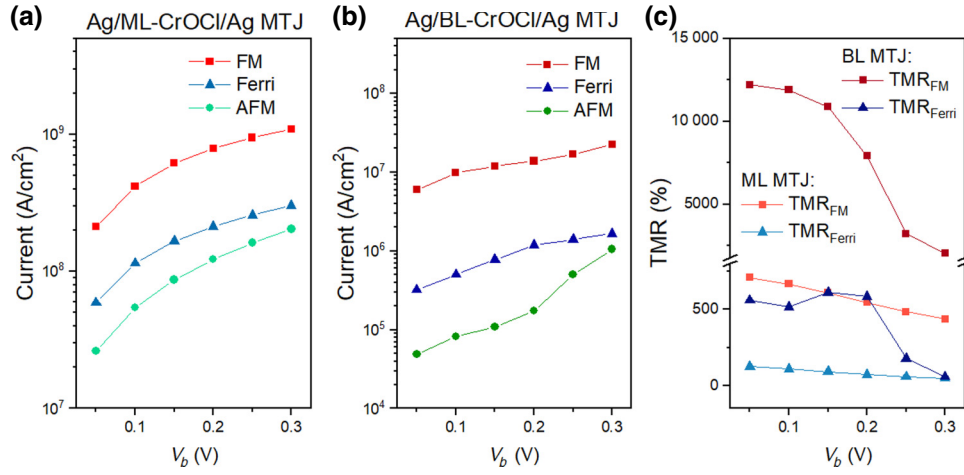


FIG. 5. (a),(b) Bias-dependent current density output under ferromagnetic and antiferromagnetic states and (c) TMR of the ML and BL CrOCl MTJs.

Therefore, the TMR_M grows along with the metamagnetic transition. Likewise, the PLDOS of the BL-CrOCl-based MTJs shows a small RA and remarkable TMR evolution (Fig. S4 in the Supplemental Material [26]). The transmission possibilities of the BL configuration drop by several orders of magnitude because of the emergent tunneling gap between two CrOCl layers (labeled by the yellow arrows in Fig. S4 in the Supplemental Material [26]).

D. Bias effect on TMR behavior

The observed TMR_{ferri} for graphite/ML CrOCl/graphite MTJ in the experiment is 140% at $V_b = 0.1$ V [17], slightly smaller than our calculated results of 205% at $V_b = 0$ V. To determine the effect of the applied bias, we calculate the IV outputs under the ferrimagnetic and the AFM states and the corresponding TMR, as shown in Fig. 5. As V_b is applied, the TMR definition becomes

$$R_{\text{TMR}}(M) = \frac{I_{\text{Ferri}} - I_{\text{AFM}}}{I_{\text{AFM}}} \times 100\%,$$

when $V_b = 0.1$ V, TMR_{ferri} drops to 111%, almost equivalent to 140% within the experiment. As V_b continues to increase from 0.15 V to 0.3 V, the current density keeps increasing while TMR_{ferri} and TMR_{FM} gradually decrease to 49% and 437%, respectively. When the magnetic tunnel barrier thickens to two layers, TMR_{ferri} becomes amplified to 4000% at zero bias, one order of magnitude higher than that in the ML case, because of the stronger spin filter effects declared in previous reports [4,9]. Followed by the rule that bias degrades TMR, TMR_{ferri} in the BL case can be as low as $\sim 500\%$ when $V_b = 0.1$ V. TMR_{ferri} of the BL CrOCl MTJ is only 5% with a large $V_b = 0.7$ V in Zhang's experimental detection [17]. The tunnel barrier thickness and the added bias offset with each other in the enhancing TMR. A thicker tunneling barrier widens

the resistance gap between the AFM and other states, thus improving the TMR. However, a thicker tunneling barrier also requires a higher bias to drive the experiment's detectable current, reducing TMR. This is the exact reason why the observed TMR_{ferri} for graphite/4-layer CrOCl/graphite MTJ exhibits only 13% in Zhang's work with the applied bias of 2.3 V. Once this bias is reduced, the TMR rises. TMR_{ferri} for graphite/4-layer CrOCl/graphite MTJ in Gu's experiment rises to $\sim 120\%$ under $V_b = 1.1$ V [16].

We also calculate the bias-dependent FM current density and TMR_{FM} (greatest TMR) of the two devices in Fig. 5. Here, I_{FM} is higher than I_{ferri} and I_{AFM} at any bias for both ML and BL cases. TMR_{FM} declines from 890% and 50 000% at zero bias to 110% and 2000% at $V_b = 0.3$ V for Ag/ML CrOCl/Ag and Ag/BL CrOCl/Ag MTJ, respectively. Due to the resource limit, we could not provide the bias-related I_{flop} and TMR_{flop} because the noncollinear-spin basis, together with bias, overburdens the current simulation condition. In terms of the magnetic evolving dynamics with fields and successive current change with bias, we infer that I_{flop} and TMR_{flop} would increase and decrease with a bias within the range between I_{ferri} and I_{AFM} and TMR_{ferri} and TMR_{FM} , respectively.

IV. TMR BENCHMARK OF 2D ANTIFERROMAGNETS

The current prosperous 2D A-type AFM family, such as CrX₃, Mn-Bi-Te, and CrSBr require more than two layers to achieve AFM-FM switching to exhibit impressive TMR when made into devices [4,39,45–48]. Monolayer CrOCl stands out by accomplishing the switching task depending on its intralayer AFM order and rich metamagnetic properties within a single layer. To assess the performance of CrOCl on TMR among the 2D AFM class, we list and

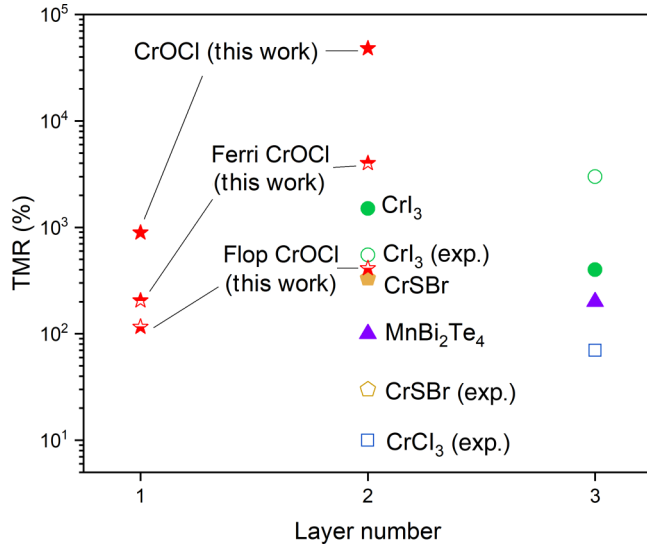


FIG. 6. Layer-dependent TMR of different 2D AFM tunnel barriers. Solid (half solid) and open dots represent calculational (this work) and experimental (exp.) results that are listed elsewhere [4,39,45–48] for comparison, respectively.

compare TMR levels in different AFM configurations, as shown in Fig. 6. The listed TMR of other AFM materials are derived from their AFM-FM switching, representing their greatest TMR. CrI₃ has the optimum TMR performance due to its recognizable high spin-polarized band dispersion [49]. Intriguingly, using only ML CrOCl yields an approachable TMR behavior ($\sim 1000\%$) to that of the BL CrI₃ (1500%). The TMR_{ferri} and the TMR_{flop} in ML CrOCl rival the theoretical TMR results for BL CrSBr [46]. It is worth noting that the experimental value from BL CrSBr is smaller than the calculations because of the additional applied voltages [47]. When the layer number increases to two, both the TMR and TMR_{ferri} of CrOCl surpass their counterparts and outperform 3-layer peers.

The tunneling evanescent states associated with the symmetry of Bloch states are examined to determine further reasons for the superior TMR of CrOCl. To establish a basis for comparison, we select CrI₃ as a reference because CrI₃ is one of the most eye-catching AFM semiconductors and has remarkable TMR in the 2D spintronic field. The TMR of bilayer and trilayer CrI₃ is 530% and 3200%, respectively, and even approaches 1 000 000% with multiple layer counterparts [5,6], all of which are much greater than other vdW antiferromagnets with the same thickness. Figure 7 plots the imaginary wave vector κ ($\mathbf{k}_z = q + i\kappa$) in bulk CrOCl and CrI₃ as an energy function at the Γ -point. Similar to the real band structures, the complex structures for the FM CrOCl and CrI₃ are also spin-dependent. The imaginary part describes the decay rate ($e^{-\kappa z}$) of the wave functions, with slower decay occurring when κ is small [50]. Because the CrOCl (and CrI₃) forms an n-type quasi-Ohmic contact with Ag electrodes, as indicated by the

PLDOS results [39], we focus on the Bloch states of their conduction band minimum. Around the CB minimum, CrOCl has more evanescent states with $\kappa < 0.5 \text{ \AA}^{-1}$ for the majority (spin-up) compared with CrI₃. Consequently, spin-up electrons propagating through CrOCl experience slower decay. Spin-down electrons with larger κ exhibit sharp evanescent for both CrOCl and CrI₃. Besides, Bloch states with low-decay rates generally have higher symmetry, with atomic orbitals aligning accordingly. For instance, s , p_z , and d_{z^2} orbitals possess the highest symmetry, followed by p_x , p_y , d_{xz} , and d_{yz} orbitals, and d_{xy} and $d_{x^2-y^2}$ orbitals having the lowest [49]. The CB minimum Bloch states of CrOCl are primarily contributed by d_{z^2} , d_{xz} , and $d_{x^2-y^2}$ of the Cr atoms, whereas those of CrI₃ are from d_{xz} , d_{yz} , and $d_{x^2-y^2}$ of the Cr atoms. The concentration of high symmetry orbitals in CrOCl under the FM state is greater ($\sim 19\%$ for the highest symmetry and $\sim 21\%$ for the second highest) compared with CrI₃ (highest at 0% and the second highest at $\sim 34\%$). When the incoming Ag states contain a mixture of s , p , and d orbitals, a slow decay of transmission through CrOCl has higher possibilities. Because electrons transmitted under the AFM state are difficult, higher transmission under the FM state results in a larger TMR. Notably, the Bloch symmetry in the magnetic tunneling region should match that of the electrodes to enhance symmetry filter effects [51].

Based on the above spin-dependent band structures, the PLDOS, and the complex bands, when the magnetic transition emerges at the ground AFM CrOCl, the gradually narrow bandgaps caused by the band edge approaching E_f , the gradually widening energy range of complete spin polarization, and the high-symmetry orbitals of the intrinsic CrOCl together contribute to its remarkable TMR in the corresponding MTJs.

V. DISCUSSION

For a high-density magnetic random-access memory (MRAM) of 5 Gbit/in², the RA of the MTJ within it should be less than 6 $\Omega \mu\text{m}^2$ [43]. This is critical for ensuring optimal memory storage density. Reducing RA is challenging, as it must be accomplished without compromising other crucial device parameters, particularly TMR, for a conventional MTJ in the commercial spin-transfer-torque-driven MRAM [52]. To the best of our knowledge, the ML CrOCl MTJ with a small RA of 0.02–0.2 $\Omega \mu\text{m}^2$ and a notable TMR of 110%–900% is very suitable for high-density applications. The small RA addresses density requirements and mitigates heat generation during current flow. This dual benefit leads to an appealing potential to significantly reduce energy consumption and minimize adverse heat effects on magnetization switching, thereby enhancing the overall endurance of the MRAM. The ML CrOCl MTJ emerges as a promising solution, offering a

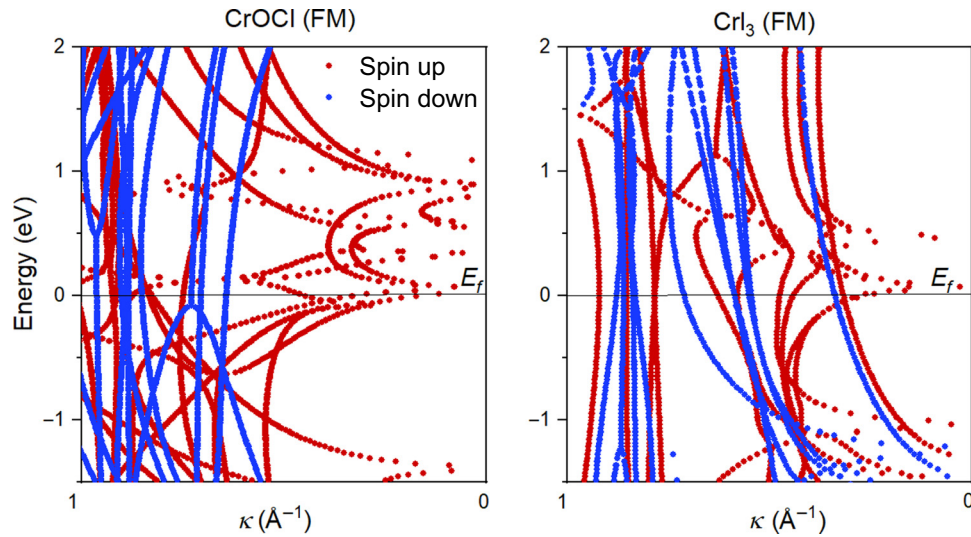


FIG. 7. Complex band structures of CrOCl and CrI₃ under FM states at the Γ -point. Dark red and blue dots are the spin-up and spin-down components, respectively. The black solid line indicates the Fermi level in their corresponding Ag/CrOCl/Ag and Ag/CrI₃/Ag MTJs.

harmonious blend of reduced RA, substantial TMR, and energy-efficient characteristics.

Moreover, the 2D CrI₃ is generally widely recognized as fragile and cannot sustain itself in air. In contrast, the favorable ambient stability of CrOCl makes it easily exfoliate into a 2D sheet, providing much simplicity in device fabrication in the experiment. Recent experimental findings have unveiled that the 4-layer CrOCl undergoes an electric phase transition accompanying the magnetic phase transition [2]. This gives us a valuable hint that the four metamagnetic resistance states we obtain in the 2D CrOCl might be further enriched as the magnetoelectric effects are considered.

We believe other isostructural compounds with ground AFM magnetic order may have analogous multistate behavior and unexplored physics. For example, detailed metamagnetic transitions are waiting to be excavated, given the similar magnetic hysteresis loops between VOCl and CrOCl [53]. The observed spin-phonon coupling effects in the 2D FeOCl might open avenues for magnetoelastic controlling approaches in devices [18]. Our investigation presents a potential paradigm for multi-RA applications, achieved solely by utilizing a single 2D AFM material.

VI. CONCLUSIONS

In summary, we introduce the concept of a multistate MTJ composed of one 2D antiferromagnet and electrodes and assess the output performance using quantum-transport calculations. As an illustrative example, we demonstrate the four distinct resistance states of CrOCl within the Ag/CrOCl/Ag MTJs. These various states exhibit an ultralow resistance area of 0.02–0.2 $\Omega \mu\text{m}^2$

in the Ag/ML CrOCl/Ag MTJs. The resistance area increases to 0.84–399 $\Omega \mu\text{m}^2$ in the Ag/BL CrOCl/Ag MTJs. Additionally, we conduct calculations for the TMR under different magnetic states and varying tunneling thicknesses. For the ML CrOCl-based MTJs, the TMR spans from 100% to 1000%, while for the BL CrOCl-based MTJs, it extends from 400% to 50 000%. Notably, the Ag/BL CrOCl/Ag MTJ has the highest TMR among devices based on other 2D antiferromagnets with the same tunneling layers. We hope that the remarkably large TMR, minimal RA product, and robust stability present in this work will stimulate further attention and application of CrOCl and its homogeneous compounds in low-power multistate storage.

ACKNOWLEDGMENT

We thank Dr. Yuxuan Peng for helpful discussions and Dr. Sheng Bi from Zhejiang Laboratory for technical support. This work was supported by the National Natural Science Foundation of China (Grants No. 12241401, No. 91964101, No. 11975035, and No. 12347160), the Key Scientific Research Project of Colleges and Universities in He'nan Province (Grant No. 24A140022), the Natural Science Foundation of He'nan Province (Grant No. 242300421671), and the High-Performance Computing Platform of Peking University.

[1] P. Qin, H. Yan, X. Wang, H. Chen, Z. Meng, J. Dong, M. Zhu, J. Cai, Z. Feng, X. Zhou, L. Liu, T. Zhang, Z. Zeng, J. Zhang, C. Jiang, and Z. Liu, Room-temperature

- magnetoresistance in an all-antiferromagnetic tunnel junction, *Nature* **613**, 485 (2023).
- [2] P. Gu, C. Wang, D. Su, Z. Dong, Q. Wang, Z. Han, K. Watanabe, T. Taniguchi, W. Ji, Y. Sun, and Y. Ye, Multistate data storage in a two-dimensional stripy antiferromagnet implemented by magnetoelectric effect, *Nat. Commun.* **14**, 3221 (2023).
- [3] Z. Wang, I. Gutiérrez-Lezama, N. Ubrig, M. Kroner, M. Gibertini, T. Taniguchi, K. Watanabe, A. Imamoğlu, E. Giannini, and A. F. Morpurgo, Very large tunneling magnetoresistance in layered magnetic semiconductor CrI₃, *Nat. Commun.* **9**, 2516 (2018).
- [4] D. R. Klein, D. MacNeill, J. L. Lado, D. Soriano, E. Navarro-Moratalla, K. Watanabe, T. Taniguchi, S. Manni, P. Canfield, J. Fernández-Rossier, and P. Jarillo-Herrero, Probing magnetism in 2D van der Waals crystalline insulators via electron tunneling, *Science* **360**, 1218 (2018).
- [5] H. H. Kim, B. Yang, T. Patel, F. Sfigakis, C. Li, S. Tian, H. Lei, and A. W. Tsen, One million percent tunnel magnetoresistance in a magnetic van der Waals heterostructure, *Nano Lett.* **18**, 4885 (2018).
- [6] T. Song, X. Cai, M. W.-Y. Tu, X. Zhang, B. Huang, N. P. Wilson, K. L. Seyler, L. Zhu, T. Taniguchi, K. Watanabe, M. A. McGuire, D. H. Cobden, D. Xiao, W. Yao, and X. Xu, Giant tunneling magnetoresistance in spin-filter van der Waals heterostructures, *Science* **360**, 1214 (2018).
- [7] Z. Wang, M. Gibertini, D. Dumcenco, T. Taniguchi, K. Watanabe, E. Giannini, and A. F. Morpurgo, Determining the phase diagram of atomically thin layered antiferromagnet CrCl₃, *Nat. Nanotechnol.* **14**, 1116 (2019).
- [8] Y. X. Peng, Z. C. Lin, G. Tian, J. Yang, P. J. Zhang, F. G. Wang, P. F. Gu, X. Y. Liu, C. W. Wang, M. Avdeev, F. Y. Liu, D. Zhou, R. Han, P. Shen, W. Y. Yang, S. Q. Liu, Y. Ye, and J. B. Yang, Controlling spin orientation and metamagnetic transitions in anisotropic van der Waals antiferromagnet CrPS₄ by hydrostatic pressure, *Adv. Funct. Mater.* **32**, 2106592 (2022).
- [9] J. Yang, S. B. Fang, Y. X. Peng, S. Q. Liu, B. C. Wu, R. G. Quhe, S. L. Ding, C. Yang, J. C. Ma, B. W. Shi, L. Q. Xu, X. T. Sun, G. Tian, C. S. Wang, J. J. Shi, J. Lu, and J. B. Yang, Layer-dependent giant magnetoresistance in two-dimensional CrPS₄ magnetic tunnel junctions, *Phys. Rev. Appl.* **16**, 024011 (2021).
- [10] L. Pan, L. Huang, M. Zhong, X.-W. Jiang, H.-X. Deng, J. Li, J.-B. Xia, and Z. Wei, Large tunneling magnetoresistance in magnetic tunneling junctions based on two-dimensional CrX₃ (X = Br, I) monolayers, *Nanoscale* **10**, 22196 (2018).
- [11] T. Zhang, Y. Wang, H. Li, F. Zhong, J. Shi, M. Wu, Z. Sun, W. Shen, B. Wei, W. Hu, X. Liu, L. Huang, C. Hu, Z. Wang, C. Jiang, S. Yang, Q.-m. Zhang, and Z. Qu, Magnetism and optical anisotropy in van der Waals antiferromagnetic insulator CrOCl, *ACS Nano* **13**, 11353 (2019).
- [12] X. Qing, H. Li, C. Zhong, P. Zhou, Z. Dong, and J. Liu, Magnetism and spin exchange coupling in strained monolayer CrOCl, *Phys. Chem. Chem. Phys.* **22**, 17255 (2020).
- [13] N. Miao, B. Xu, L. Zhu, J. Zhou, and Z. Sun, 2D intrinsic ferromagnets from van der Waals antiferromagnets, *J. Am. Ceram. Soc.* **140**, 2417 (2018).
- [14] F. Zhang, Y.-C. Kong, R. Pang, L. Hu, P.-L. Gong, X.-Q. Shi, and Z.-K. Tang, Super-exchange theory for polyvalent anion magnets, *New J. Phys.* **21**, 053033 (2019).
- [15] P. G. Reuvekamp, *Investigation into the Magnetic and the Structural Properties of Two Low-Dimensional Antiferromagnets TiPO₄ and CrOCl* (University of Stuttgart, Stuttgart, 2014).
- [16] P. Gu, *et al.*, Magnetic phase transitions and magnetoelastic coupling in a two-dimensional stripy antiferromagnet, *Nano Lett.* **22**, 1233 (2022).
- [17] M. Zhang, Q. Hu, Y. Huang, C. Hua, M. Cheng, Z. Liu, S. Song, F. Wang, H. Lu, P. He, G.-H. Cao, Z.-A. Xu, Y. Lu, J. Yang, and Y. Zheng, Spin-lattice coupled metamagnetism in frustrated van der Waals magnet CrOCl, *Small* **19**, 2300964 (2023).
- [18] Y. Zeng, P. Gu, Z. Zhao, B. Zhang, Z. Lin, Y. Peng, W. Li, W. Zhao, Y. Leng, P. Tan, T. Yang, Z. Zhang, Y. Song, J. Yang, Y. Ye, K. Tian, and Y. Hou, 2D FeOCl: A highly in-plane anisotropic antiferromagnetic semiconductor synthesized via temperature-oscillation chemical vapor transport, *Adv. Mater.* **34**, 2108847 (2022).
- [19] J. Angelkort, A. Wölfel, A. Schönleber, S. van Smaalen, and R. K. Kremer, Observation of strong magnetoelastic coupling in a first-order phase transition of CrOCl, *Phys. Rev. B* **80**, 144416 (2009).
- [20] J. Zhang, PhD thesis, University of Bayreuth, 2014.
- [21] G. Kresse and J. Furthmüller, Efficient iterative schemes for ab initio total-energy calculations using a plane-wave basis set, *Phys. Rev. B* **54**, 11169 (1996).
- [22] J. P. Perdew, K. Burke, and M. Ernzerhof, Generalized gradient approximation made simple, *Phys. Rev. Lett.* **77**, 3865 (1996).
- [23] G. Kresse and J. Furthmüller, Efficiency of ab-initio total energy calculations for metals and semiconductors using a plane-wave basis set, *Comput. Mater. Sci.* **6**, 15 (1996).
- [24] Y. Wang, S. Liu, Q. Li, R. Quhe, C. Yang, Y. Guo, X. Zhang, Y. Pan, J. Li, H. Zhang, L. Xu, B. Shi, H. Tang, Y. Li, J. Yang, Z. Zhang, L. Xiao, F. Pan, and J. Lu, Schottky barrier heights in two-dimensional field-effect transistors: from theory to experiment, *Rep. Prog. Phys.* **84**, 056501 (2021).
- [25] J. P. Allen and G. W. Watson, Occupation matrix control of d- and f-electron localisations using DFT + U, *Phys. Chem. Chem. Phys.* **16**, 21016 (2014).
- [26] See Supplemental Material at <http://link.aps.org/supplemental/10.1103/PhysRevApplied.22.014017> for calculation details and comparison, and electronic properties and magnetism of the Ag/CrOCl interface and the corresponding device. The Supplemental Materials also contains Refs. [15–17,24,25,33].
- [27] M. Brandbyge, J.-L. Mozos, P. Ordejón, J. Taylor, and K. Stokbro, Density-functional method for nonequilibrium electron transport, *Phys. Rev. B* **65**, 165401 (2001).
- [28] D. Supriyo, *Electronic Transport in Mesoscopic System* (Cambridge University Press, Cambridge, 1995).
- [29] J. Yang, B. Wu, J. Zhou, J. Lu, J. Yang, and L. Shen, Full electrical control of multiple resistance states in van der Waals sliding multiferroic tunnel junctions, *Nanoscale* **15**, 16103 (2023).

- [30] D. Supriyo, *Quantum Transport: Atom to Transistor* (Cambridge University Press, Cambridge, 2005).
- [31] J. Chen, Y. Guo, C. Ma, S. Gong, C. Zhao, T. Wang, X. Dong, Z. Jiao, S. Ma, G. Xu, and Y. An, Magnetic nanodevices and spin-transport properties of a two-dimensional CrSCl monolayer, *Phys. Rev. Appl.* **19**, 054013 (2023).
- [32] R. Wu, A. Ross, S. Ding, Y. Peng, F. He, Y. Ren, R. Lebrun, Y. Wu, Z. Wang, J. Yang, A. Brataas, and M. Kläui, Magnetotransport study of van der Waals CrPS₄/(Pt,Pd) heterostructures: Spin-flop transition and room-temperature anomalous Hall effect, *Phys. Rev. Appl.* **17**, 064038 (2022).
- [33] Y. Peng, S. Ding, M. Cheng, Q. Hu, J. Yang, F. Wang, M. Xue, Z. Liu, Z. Lin, M. Avdeev, Y. Hou, W. Yang, Y. Zheng, and J. Yang, Magnetic structure and metamagnetic transitions in the van der Waals antiferromagnet CrPS₄, *Adv. Mater.* **32**, 2001200 (2020).
- [34] S. W. Jang, D. H. Kiem, J. Lee, Y.-G. Kang, H. Yoon, and M. J. Han, Hund's physics and the magnetic ground state of CrOX (X = Cl, Br), *Phys. Rev. Mater.* **5**, 034409 (2021).
- [35] S. S. P. Parkin, C. Kaiser, A. Panchula, P. M. Rice, B. Hughes, M. Samant, and S. H. Yang, Giant tunnelling magnetoresistance at room temperature with MgO (100) tunnel barriers, *Nat. Mater.* **3**, 862 (2004).
- [36] P. Bose, P. Zahn, J. Henk, and I. Mertig, Tailoring tunnel magnetoresistance by ultrathin Cr and Co interlayers: A first-principles investigation of Fe/MgO/Fe junctions, *Phys. Rev. B* **82**, 014412 (2010).
- [37] Y. Wang, R. Fei, R. Quhe, J. Li, H. Zhang, X. Zhang, B. Shi, L. Xiao, Z. Song, J. Yang, J. Shi, F. Pan, and J. Lu, Many-body effect and device performance limit of monolayer InSe, *ACS Appl. Mater. Interfaces* **10**, 23344 (2018).
- [38] S. Smidstrup, *et al.*, QuantumATK: an integrated platform of electronic and atomic-scale modelling tools, *J. Phys.: Condens. Matter* **32**, 015901 (2020).
- [39] B. Wu, J. Yang, R. Quhe, S. Liu, C. Yang, Q. Li, J. Ma, Y. Peng, S. Fang, J. Shi, J. Yang, J. Lu, and H. Du, Scaling behavior of magnetoresistance with the layer number in CrI₃ magnetic tunnel junctions, *Phys. Rev. Appl.* **17**, 034030 (2022).
- [40] Z. Yan, R. Zhang, X. Dong, S. Qi, and X. Xu, Significant tunneling magnetoresistance and excellent spin filtering effect in CrI₃-based van der Waals magnetic tunnel junctions, *Phys. Chem. Chem. Phys.* **22**, 14773 (2020).
- [41] J. G. Deak, Z. M. Zhou, and W. F. Shen, Tunneling magnetoresistance sensor with pT level 1/f magnetic noise, *AIP Adv.* **7**, 056676 (2017).
- [42] X. Dong, X. Shen, X. Sun, Y. Bai, Z. Yan, and X. Xu, Voltage-tunable giant nonvolatile multiple-state resistance in sliding-interlayer ferroelectric h-BN van der Waals multiferroic tunnel junction, *Phys. Rev. B* **108**, 085427 (2023).
- [43] Y. Su, X. Li, M. Zhu, J. Zhang, L. You, and E. Y. Tsymlal, Van der Waals multiferroic tunnel junctions, *Nano Lett.* **21**, 175 (2021).
- [44] J. Han, C. Lv, W. Yang, X. Wang, G. Wei, W. Zhao, and X. Lin, Large tunneling magnetoresistance in van der Waals magnetic tunnel junctions based on FeCl₂ films with interlayer antiferromagnetic couplings, *Nanoscale* **15**, 2067 (2023).
- [45] G. Zhan, Z. Yang, K. Luo, D. Zhang, W. Lou, J. Liu, Z. Wu, and K. Chang, Spin-dependent tunneling in 2D MnBi₂Te₄-based magnetic tunnel junctions, *MRS Bull.* **47**, 1177 (2022).
- [46] H. Liu, Y.-Y. Liu, H. Wen, H. Wu, Y. Zong, J. Xia, and Z. Wei, Spin-filter magnetic tunnel junctions based on A-type antiferromagnetic CrSBr with giant tunnel magnetoresistance, *Magnetochemistry* **8**, 89 (2022).
- [47] E. J. Telford, *et al.*, Coupling between magnetic order and charge transport in a two-dimensional magnetic semiconductor, *Nat. Mater.* **21**, 754 (2022).
- [48] D. R. Klein, D. MacNeill, Q. Song, D. T. Larson, S. Fang, M. Xu, R. A. Ribeiro, P. C. Canfield, E. Kaxiras, R. Comin, and P. Jarillo-Herrero, Enhancement of interlayer exchange in an ultrathin two-dimensional magnet, *Nat. Phys.* **15**, 1255 (2019).
- [49] T. R. Paudel and E. Y. Tsymlal, Spin filtering in CrI₃ tunnel junctions, *ACS Appl. Mater. Interfaces* **11**, 15781 (2019).
- [50] Y. Su, J. Zhang, J.-T. Lü, J. Hong, and L. You, Large magnetoresistance in an electric-field-controlled antiferromagnetic tunnel junction, *Phys. Rev. Appl.* **12**, 044036 (2019).
- [51] W. H. Butler, Tunneling magnetoresistance from a symmetry filtering effect, *Sci. Technol. Adv. Mater.* **9**, 014106 (2008).
- [52] C. Park, H. Lee, C. Ching, J. Ahn, R. Wang, M. Pakala, and S. H. Kang, in *IEEE Symposium on Vlsi Technology* (2018), pp. 185–186.
- [53] W. J. Wang, R. Sun, S. J. He, Z. Y. Jia, C. L. Su, Y. Li, and Z. C. Wang, Atomic structure, work function and magnetism in layered single crystal VOCl, *2D Mater.* **8**, 015027 (2021).